Submitted as a Short Communication to *Journal of the European Ceramic Society*, April 2020. Revised May 2020.

Pressureless ultrafast sintering of near-net-shaped superhard isotropic B_4C/rGO composites with Ti-Al additives

Cristina Ojalvo [a], Rodrigo Moreno [b], Fernando Guiberteau [a], Angel L. Ortiz [a,*]

[a] Departamento de Ingeniería Mecánica, Energética y de los Materiales,
Universidad de Extremadura, 06006 Badajoz, Spain.

[b] Instituto de Cerámica y Vidrio, Consejo Superior de Investigaciones Científicas,
Madrid 28049, Spain.

Abstract

Superhard composites of B_4C reinforced with randomly-oriented reduced graphene oxide (rGO) nanoplatelets are manufactured by a near-net-shape fabrication route based on three successive steps. Firstly, aqueous colloidal processing is used for the environmentally-friendly preparation of a semi-concentrated multi-component slurry (B_4C as main component, Ti-Al as sintering additive, and rGO as toughening reinforcement), whose suitability for wet shaping is demonstrated by rheological measurements. Secondly, slip casting is used to produce robust green parts with shapes on demand and microstructures free of macro- and micro-defects. And thirdly, pressureless spark-plasma sintering (PSPS) is used for the ultrafast and energy-efficient densification of the green parts with shape retention. Measurements of shrinkage and hardness, as well as the microstructural observations, are used to identify suitable PSPS temperatures leading to obtaining isotropic B_4C/rGO composites that are superhard and almost twice as tough as the monolithic B_4C ceramics.

Keywords: B_4C; aqueous colloidal processing; slip casting; pressureless spark-plasma sintering; mechanical properties.

* Corresponding author:

Angel L. Ortiz
Phone: +34 924289600 Ext: 86726
Fax: +34 924289601
E-mail: alortiz@unex.es

1. Introduction

There has been growing interest lately in reinforcing the microstructure of the otherwise brittle polycrystalline ceramics with graphene-like nanoplatelets (GNPs) to thus improve their low fracture toughness by crack-bridging mechanisms [1-8]. (The term GNPs is imprecise, and includes nanoplatelets of graphene oxide (GO), of partially reduced graphene oxide (prGO), and of reduced graphene oxide (rGO), but not of graphite. Also, they are multi-layer, not single-layer, two-dimensional materials.) Rather than carbon nanotubes (CNTs), GNPs are currently preferable as reinforcements because their two-dimensional nature makes them in principle more effective in bridging cracks [9], and they are also more easily dispersible in ceramic matrices [8,10]. This interest includes monolithic B_4C ceramics which are very brittle, and have, regardless of the grain size, a low fracture toughness of only ~2 MPa· $m^{1/2}$ [11] that can compromise their mechanical integrity in service thus limiting in practice their great potential as superhard materials. Unsurprisingly, to make them less susceptible to failure, B_4C/GNP composites, often B_4C/rGO composites, are being fabricated by spark-plasma sintering (SPS) or hot pressing (HP) [12-21]. The former is preferable over the latter because ultrafast sintering avoids the more than likely graphitization of the GNPs under prolonged exposure to high temperatures.

Interestingly, B_4C/GNP composites can have either orthotropic or isotropic microstructures [12-21] depending on whether during sintering the GNP reinforcements align perpendicularly to the pressing direction or remain randomly oriented. The microstructural design, fortuitous or not, nonetheless conditions the mechanical performance because the orthotropic composites exhibit a pronouncedly rising *R*-curve [22], indicative of marked toughening, in the direction perpendicular to the GNP reinforcements but with no toughening in

the direction parallel to them, whilst the isotropic composites exhibit a relatively shallow *R*-curve [22], indicative of moderate toughening, in any direction. Therefore, the orthotropic B_4C/GNP composites will perform especially well in those structural applications under uniaxial loading where the cracks, once nucleated, are forced to propagate perpendicularly to the GNPs, but badly under multi-axial loading where cracks can propagate in any direction. In this last scenario, isotropic B_4C/GNP composites are doubtless much more recommendable.

Another handicap of the orthotropic B_4C/GNP composites is that they have little capacity to meet the demand for parts with ever more complex geometries required by industry because the preferential alignment of the GNPs is achieved thanks to the application of uniaxial pressure during sintering. This fabrication procedure limits the geometry of the parts fabricated to just simple shapes, and the fact is that the extensive post-sintering machining and finishing operations on B_4C-based materials are prohibitively expensive and time-consuming, not to say completely inviable in most cases. Unlike the orthotropic B_4C/GNPs composites, the fabrication of isotropic B_4C/GNPs composites does not require the application of pressure, and therefore, in principle, they are amenable to near-net-shape manufacturing. In particular, isotropic B_4C/GNP composites could first be shaped into geometrically-complex parts by wet-forming techniques, and then these green parts densified by pressureless SPS (PSPS). This last ensures ultrafast densification, and also the preservation of both the external shape given to the piece during casting and its isotropic microstructure. However, pressureless densification of B_4C constitutes another challenge to its poor sinterability [23,24], both intrinsic (strong covalent bonding and low self-diffusion coefficients imposing serious kinetics restrictions) and extrinsic (oxidic impurities favouring microstructural coarsening over densification). To promote the pressureless densification of B_4C, sintering additives are required, and those forming transient liquid phases

are currently gaining in interest [25-29].

The present study was aimed in this direction, and was undertaken to explore the possible processability of superhard isotropic B_4C/rGO composites with shape on demand by combining aqueous slip casting for the environmentally-friendly preparation of green parts with the desired geometry, and PSPS with Ti-Al transient liquid-phase additives [25-27] for their ultrafast and energy-efficient densification. The study is thus aimed at contributing towards the near-net-shape manufacture of advanced B_4C composites for engineering applications.

2. Experimental Procedure

Ceramic slurries were prepared by aqueous colloidal processing, using de-ionized water as dispersant, commercial powders of B_4C (d_{50} ~ 0.7 μm; Grade HD 20, H.C. Starck, Germany), Ti-Al (d_{50} ~ 38 μm; 22895, Alfa Aesar, Germany), and prGO (5 μm diameter and 2 nm thickness; 2.1, Abalonyx AS, Norway) as solids, and a commercial polyethylenimine (PEI; MW ~ 25 000; Sigma-Aldrich, USA) as deflocculant. The B_4C, Ti-Al, and prGO powders were used as-received, while PEI was used diluted to 20 vol.% in de-ionized water. Also note that prGO will further reduce to rGO in situ during ultrafast sintering [21]. The slurry was formulated to a total solids loading of 20 vol.%, and was designed to yield B_4C composites with 4.9 vol.% Ti-Al and 2 vol.% rGO (implying a composition in wt.% of 89.82B_4C+7.08Ti-Al+3.10prGO).

The slurries were prepared under continuous mechanical agitation with helices at 310 rpm, according to the following recipe for 100 ml optimized in an earlier study [21]. First, 0.49 ml of diluted PEI were added to 74.44 ml of de-ionized water to deflocculate the prGO powder, and 1 min later 1.63 g of prGO powder was gradually incorporated. (This amount of prGO takes into account that the present prGO loses ~42.49 wt.% when reducing to rGO in situ during SPS

[21].) After 5 min, 5.07 ml of diluted PEI was added to deflocculate both the Ti-Al and the B_4C powders; 1 min later 3.71 g of Ti-Al was introduced; and 15 min later 46.95 g of B_4C was gradually added. The slurry's pH was then adjusted to 7 (i.e., to neutral pH). Finally, after a further 30 min, the slurry was sonicated (UP-400S, Hielscher Ultrasonics GmbH, Germany) with pulses of 240 W (0.5 s of power discharge and 0.5 s of pause) for 2 min. The resulting slurry was then characterized rheologically to measure its viscosity, using a rheometer (MARS, Haake, Thermo, Germany) configured in the double cone-plate geometry and operated in controlled shear rate mode.

Next, the slurry was slip cast in bottomless plastic moulds (greased with wax) of cylindrical shape placed on top of a permeable, flat, plaster-of-Paris plate to obtain compact discs, which were allowed to dry in air at room temperature for 48 h within the moulds. Their green microstructure was then examined by scanning electron microscopy (SEM; Quanta 3D, FEI, The Netherlands) on fracture surfaces. The green discs were cold isostatically pressed at 150 MPa, and measured carefully to evaluate their dimensions. Note that isostatic pressing does not cause shape distortion, and promotes a greater green compaction that is essential for B_4C pieces to densify satisfactorily, as has been demonstrated elsewhere [30]. Lastly, as shown in Fig. 1, the isostatically-pressed green discs were individually loaded into a special graphite die designed to avoid load application, which is lined with graphite foil and covered by a graphite felt, and were PSPS-ed (HP-D-10, FCT Systeme GmbH, Germany) in a dynamic-vacuum atmosphere at 1900°C, 1950°C, 2000°C, 2050°C, and 2100°C (as measured using an axial optical pyrometer) for 5 min, under 100°C/min heating. Higher sintering temperatures were not used to prevent damage of the SPS furnace. The sintered discs were re-measured to evaluate the degree of shrinkage occurring during sintering, and were characterized microstructurally by SEM

on fracture surfaces and mechanically by Vickers indentation (MV-1, Matsuzawa, Japan) under 9.8 N load on polished surfaces.

3. Results and Discussion

Figure 2 shows the viscosity curve (i.e., viscosity vs shear rate) of the optimal slurry of B_4C+Ti-Al+prGO prepared by aqueous colloidal processing as explained above, demonstrating that it has the fluidity required for slip casting. Clearly, it can be seen that this slurry has the desired shear-thinning rheological behaviour with little thixotropy, exhibiting a high (exponentially-increasing) viscosity under rest conditions that avoids particle settling during both its storage and its casting, but a much lower viscosity under flow conditions that facilitates its pumping and the mould filling [31-33]. Indeed, it is widely agreed that for a slurry to be well-suited for slip casting operations it has to have a viscosity lower than ~1 Pa· s at a shear rate of 100 s^{-1} because otherwise it cannot be poured appropriately [34]. As can be seen in Fig. 2, the slurry of B_4C+Ti-Al+prGO prepared in this study amply meets that requirement, with its viscosity at 100 s^{-1} of ~0.04 Pa· s being two orders of magnitude lower than the recommended upper limit [34]. The visual observation also shown in Fig. 2 confirmed that this slurry is indeed very fluid, which is also indicative that it has the sought-for good dispersion of the B_4C, Ti-Al, and prGO.

Figure 3 shows optical photographs of the green parts obtained by pouring the slurry into cylindrical moulds without external suction, followed by drying in air at room temperature for 48 h. Most were disc-shaped because this morphology facilitates the subsequent measurement of the shrinkages occurring during sintering. Clearly, these images confirm the expectation that the slurry prepared here to a total solids loading of 20 vol.% is very suitable for the slip casting of

green parts with the desired geometry as dictated simply by the mould design. Note that, for slip casting, concentrated slurries with high total solids loadings are not required, but that, what are needed are only semi-concentrated slurries with moderate total solids loadings. This is because in slip casting, unlike other direct forming techniques, the stages of shaping, consolidation, and drying take place concurrently since draining occurs by filtration in the permeable mould, and the lower viscosity of the moderately concentrated slurries is very beneficial for making complex parts. Also importantly, the inspection and control of the green discs indicated that (*i*) they had no external macro-defects (cracks, surface voids, colour changes, swelling, etc.), (*ii*) they were robust, (*iii*) they had good handling and storage characteristics, and (*iv*) they were trimmable in dry conditions.

Figure 4 shows an SEM image representative of the fracture surface of the as-cast compacts (prior to isostatic pressing) in which it can be seen that they have a uniform green microstructure with both a homogeneous distribution and good packing of particles as well as no internal macro-defects (large cracks, voids, etc.) or micro-defects (large pores, particle size segregation, small cracks, laminations, packing gradients, etc.). Interestingly, the green microstructures show fine Ti-Al particles here and there (brighter particles), whose maximum size of only a few microns is much less than the ~38 μm of the starting Ti-Al particles, indicative that the 2 min of sonication applied during the aqueous colloidal processing of the slurry broke up the large starting Ti-Al agglomerates. Sonication also seems to have re-exfoliated the prGO platelets, making them, in general, thinner and shorter than the flaky starting prGO platelets. Thus, the green microstructures have the desired better dispersion of the Ti-Al sintering additive and prGO reinforcements between the B_4C particles, which should doubtless be beneficial for the pressureless sinterability of B_4C/rGO composites with uniform isotropic microstructures.

Figure 5 shows the linear and volume shrinkages that occurred during sintering relative to the isostatically-pressed green discs (which have a relative density of ~61%). As expected, it was observed that the discs shrank isotropically thus retaining their shape given during slip casting, undergoing increasing linear shrinkages from ~9.5% when sintered at 1900°C up to ~13.2% when sintered at 2100°C. Accordingly, the volume shrinkage gradually increased from ~27% up to ~35% as the sintering temperature increased from 1900°C to 2100°C.

Figure 6 shows SEM images representative of the fracture surface of the discs sintered at temperatures between 1900°C and 2100°C. As can be observed, the disc sintered at 1900°C (Fig. 6A) is poorly densified, and has an inhomogeneous fine-grained microstructure dominated by large, very porous regions together with small, dense regions formed by only a few submicrometre grains. Grain sizes are thus essentially the same as the particle sizes in the starting B_4C powder (~ 0.7 μm). There are also rGO platelets all over the microstructure. This disc is thus in a very incipient state of densification, having reached, if at all, just the early stage of the intermediate sintering regime. The microstructure of the disc sintered at 1950°C (Fig. 6B) is similar in qualitative terms, overall with the same submicrometre grain size (~ 0.7 μm), but quantitatively it has much less porosity and somewhat larger well-densified regions. It therefore had reached the middle stage of the intermediate sintering regime. The disc sintered at 2000°C (Fig. 6C) is only moderately porous, and its microstructure exhibits partially-densified regions with fine grains (< 1 μm) and irregular pores plus well-densified regions (~ 10 μm) with coarser grains and relatively spherical pores. It therefore seems that these dense regions were formed because the formerly fine grains within the small dense regions grew, and then coalesced leaving some pores entrapped. Hence, the disc sintered at 2000°C had already reached the later stage of the intermediate sintering regime. The microstructure of the disc sintered at 2050°C (Fig. 6D) is

different, without the partially-dense regions observed before and with coarser grains (apparently one ten of microns in size) and rGO platelets here and there. The occurrence of notable microstructural coarsening above certain PSPS temperature is not however a surprise because it has been already observed for B_4C monolithics fabricated by SPS [11,35]. Some pores are very spherical (internal pores), while others have irregular (corner pores) or lenticular (edge/face pores) shapes. This disc had thus reached the early stage of the final sintering regime. Lastly, the disc sintered at 2100°C (Fig. 6E) is near-fully dense (with only a few spherical pores), and its microstructure has even coarser grains (apparently several tens of microns in size) and randomly-oriented rGO platelets. This last is more evident in the higher-magnification SEM image of Fig. 7 in which some rGO platelets are more easily distinguishable (some other second phases are intuited as well). The disc sintered at 2100°C had thus reached the desired later stage of the final sintering regime.

It is also important to mention that while the green parts contain prGO platelets and Ti-Al intermetallic particles, the PSPS-ed composites contain however rGO platelets and TiB_2 and Al_4C_3 particles. The former is because prGO further reduces thermally in situ during SPS to rGO, as demonstrated by Raman spectroscopy [21]. Also note that the rGO reinforcements, like other flaky [36] and non-flaky [37-39] reinforcements, retard grain growth and hinder densification because they are obstacles to the diffusion [22]. The latter is because Ti-Al is a transient liquid phase sintering additive that during SPS first melts helping in densification, and then this liquid reacts with part of the B_4C ($6B_4C+4Ti_3Al \rightarrow 12TiB_2+Al_4C_3+3C$ and $B_4C+4TiAl+C \rightarrow 4TiB_2+Al_4C_3$) [25-27], disappearing. Therefore, strictly speaking, these are not only, but essentially, B_4C/rGO composites. The importance of using the Ti-Al additives becomes comparatively evident considering that the green parts prepared from the B_4C powders by cold-

uniaxial pressing at 50 MPa plus cold-isostatic pressing at 200 MPa and then PSPS-ed at 2100°C are quite porous, having reached only the later stage of the intermediate sintering regime [30].

Figure 8 shows the hardness of the resulting isotropic B_4C/rGO composites as a function of the sintering temperature. It can be seen that hardness increases exponentially from ~8 GPa up to ~30.5 GPa with increasing sintering temperature from 1900°C up to 2100°C. Thus, as expected, hardness correlates inversely with the residual porosity [11], rising with the increase of densification. The discs sintered at or below 2000°C are very soft (to be B_4C composites), attributable to their not even having reached the final sintering regime. The disc sintered at 2050°C has the hardness typical of the B_4C ceramics fabricated by conventional pressureless sintering (~18-24 GPa) [23], but with the advantage that its sintering time is less than 30 min instead of several hours. To put this hardness value in perspective, it must be noted that this porous B_4C/rGO composite is harder, or much harder, than the typical well-densified structural oxide ceramics – ZrO_2 (~14 GPa), Al_2O_3 (~18 GPa), etc. Lastly, the disc sintered at 2100°C has the super-hardness above 30 GPa desired for the B_4C-based materials, being indeed much harder than the monolithic B_4C ceramics fabricated by PSPS (~14.9±1.3 GPa) [30] and only slightly softer than the monolithic B_4C ceramics with coarse-grained microstructures (~17 μm grain size) fabricated by SPS under pressure of 75 MPa, these last with a hardness of ~33 GPa [11]. This slight hardness difference (~2.5 GPa) is due simply to the low residual porosity, the Ti-Al sintering additives, and the rGO platelets that together reduce the hardness of the B_4C/rGO composite relative to the monolithic B_4C ceramic. However, with both materials having coarse-grained microstructures, the present super-hard B_4C/rGO composite is, as intended, tougher than the monolithic B_4C ceramics since the former reaches a fracture toughness as high as ~3.9 MPa· $m^{1/2}$ which is essentially twice as high as that of the latter (~2 MPa· $m^{1/2}$ [11]). This

excellent combination of super-hardness and enhanced fracture toughness, together with the feasibility of successfully fabricating geometrically-complex parts with near-net shape, make these isotropic B_4C/rGO composites especially appealing for a myriad of engineering applications.

Nonetheless, it would be ideal if these near-net-shaped B_4C/rGO composites were to have finer-grained microstructures, which perhaps could be achievable in future studies making some adjustments to the fabrication route followed here. For example, implementing more complex PSPS cycles could minimize the exposure times within the intermediate temperature range responsible for grain coarsening without densification. Also, preparing non-aqueous slurries in methanol, albeit not environmentally-friendly, would cleanse the B_4C particles of the detrimental surface oxides that promote grain coarsening [40,41]. And finally, imposing electrical contact between the punches and the green parts during PSPS would result in a pulsed electrical current circulating through the compact, thus favouring densification with less grain coarsening.

4. Concluding Remarks

We have demonstrated that it is possible to fabricate superhard, toughened B_4C/rGO composites with isotropic microstructures by combining aqueous slip casting and pressureless spark-plasma sintering. In particular, we have shown that the former enables the environmentally-friendly preparation of slurries with shear-thinning rheological behaviour, low viscosity, and little thixotropy to obtain robust green parts with shape on demand and microstructures free of macro- and micro-defects, and that the latter enables the ultrafast densification of these green parts while retaining their shape. Also, thanks to the measurement of shrinkages and hardnesses, as well as to the microstructural observations, we have identified

sintering temperatures suitable for obtaining superhard isotropic B_4C/rGO composites with enhanced fracture toughness relative to monolithic B_4C ceramics.

Acknowledgements. This work was supported by the Ministerio de Economía y Competitividad (Government of Spain) and FEDER Funds under the Grants nº MAT2016-76638-R and RTI2018-099033-B-C33. Financial support from the Junta de Extremadura under the Grant nº GR18149, also co-financed with FEDER Funds, is gratefully acknowledged as well. The authors thank Abalonyx AS for kindly providing the prGO starting powders. Cristina Ojalvo thanks the Junta de Extremadura for funding her PhD Grant nº PD16027. Thanks are also due to Carmen Alcázar and María Díaz, at the Instituto de Cerámica y Vidrio, for their technical assistance.

References

1. K. Wang, Y. Wang, Z. Fan, J. Yan, T. Wei, Preparation of graphene nanosheet/alumina composites by spark plasma sintering, Mater. Res. Bull 46 [2] (2011) 315–318.
2. L.S. Walker, V.R. Marotto, M.A. Rafiee, N. Koratkar, E.L. Corral, Toughening in graphene ceramic composites, ACS Nano 5 [4] (2011) 3182–3190.
3. J. Liu, H.X. Yan, M.J. Reece, K. Jiang, Toughening of zirconia/alumina composites by the addition of graphene platelets, J. Eur. Ceram. Soc. 32 [16] (2012) 4185–4193.
4. C. Ramirez, P. Miranzo, M. Belmonte, M.I. Osendi, P. Poza, S.M. Vega-Diaz, M. Terrones, Extraordinary toughening enhancement and flexural strength in Si_3N_4 composites using graphene sheets, J. Eur. Ceram. Soc. 34 [2] (2014) 161–169.
5. H.J. Kim, S.M. Lee, Y.S. Oh, Y.H. Yang, Y.S. Lim, D.H. Yoon, C. Lee, J.Y. Kim, R.S. Ruoff, Unoxidized graphene/alumina nanocomposite: fracture-and wear-resistance effects of graphene on alumina matrix, Sci. Rep. 4 (2014) 5176.
6. S.N. Alam, N. Sharrma, B.C. Ray, S. Yadav, K. Biswas, Effect of graphite nanoplatelets on the mechanical properties of alumina-based composites, Ceram. Int. 43 [14] (2017) 11376–11389.
7. A. Nieto, A. Bisht, D. Lahiri, C. Zhang, A. Agarwal, Graphene reinforced metal and ceramic matrix composites: a review, Int. Mater. Rev. 62 [5] (2017) 241–302.
8. P. Miranzo, M. Belmonte, M.I. Osendi, From bulk to cellular structures: a review on ceramic/graphene filler composites, J. Eur. Ceram. Soc. 37 [12] (2017) 3649–3672.
9. C. Ramirez, Q. Wang, M. Belmonte, P. Miranzo, M.I. Osendi, B.W. Sheldon, N.P. Padture, Direct in situ observation of toughening mechanisms in nanocomposites of silicon nitride and reduced graphene-oxide, Scripta Mater 149 (2018) 40–43.

10. M. Belmonte, P. Miranzo, M.I. Osendi, Contact damage resistant SiC/graphene nanofiller composites, J. Eur. Ceram. Soc. 38 [1] (2018) 41–45.
11. B.M. Moshtaghioun, D. Gómez-García, A. Domínguez-Rodríguez, R.I. Todd, Grain size dependence of hardness and fracture toughness in pure near fully-dense boron carbide ceramics, J. Eur. Ceram. Soc. 36 [7] (2016) 1829–1834.
12. M. Li, W. Wang, Q. He, A. Wang, L. Hu, Z. Fu, Reduced-graphene-oxide-reinforced boron carbide ceramics fabricated by spark plasma sintering from powder mixtures obtained by heterogeneous co-precipitation, Ceram. Int. 45 [13] (2019) 16496–16503.
13. L. Hu, W. Wang, Q. He, A. Wang, C.Liu, T. Tian, H. Wang, Z. Fu, Preparation and characterization of reduced graphene oxide-reinforced boron carbide ceramics by self-assembly polymerization and spark plasma sintering, J. Eur. Ceram. Soc. 40 [3] (2020) 612–621.
14. A. Kovalčíková, R. Sedlák, P. Rutkowski, J. Dusza, Mechanical properties of boron carbide+graphene platelet composites, Ceram. Int. 42 [1 Part B] (2016) 2094–2098.
15. R. Sedlák, A. Kovalčíková, J. Balko, P. Rutkowski, A. Dubiel, D. Zientara, V. Girman, E. Múdra, J. Dusza, Effect of graphene platelets on tribological properties of boron carbide ceramic composites, Int. J. Refract. Met. Hard Mater. 65 (2017) 57–63.
16. R. Sedlák, A. Kovalčíková, E. Múdra, P. Rutkowski, A. Dubiel, V. Girman, R. Bystrický, J. Dusza, Boron carbide/graphene platelet ceramics with improved fracture toughness and electrical conductivity, J. Eur. Ceram. Soc. 37 [12] (2017) 3773–3780.
17. P. Rutkowski, A. Dubiel, W. Piekarczyk, M. Ziabka, J. Dusza, Anisotropy in thermal properties of boron carbide-graphene platelet composites, J. Eur. Ceram. Soc. 36 [12] (2015) 3051–3057.

18. R. Alexander, T.S.R.Ch. Murthy, K.V. Ravikanth, J. Prakash, T. Mahata, S.R. Bakshi, M. Krishnan, K. Dasgupta, Effect of graphene nano-platelet reinforcement on the mechanical properties of hot pressed boron carbide based composite, Ceram. Int. 44 [8] (2018) 9830–9838.
19. Y. Tan, H. Luo, H. Zhang, S. Peng, Graphene nanoplatelets reinforced boron carbide composites with high electrical and thermal conductivity, J. Eur. Ceram. Soc. 36 [11] (2016) 2679–2687.
20. Y. Tan, H. Zhang, S. Peng, Electrically conductive graphene nanoplatelet/boron carbide composites with high hardness and toughness, Scripta Mater. 114 (2016) 98–102.
21. C. Ojalvo, R. Moreno, F. Guiberteau, A.L. Ortiz, Processing of orthotropic and isotropic superhard B_4C composites reinforced with reduced graphene oxide, J. Eur. Ceram. Soc. (2020), in press.
22. Q. Wang, C. Ramirez, C.S. Watts, O. Borrero-Lopez, A.L. Ortiz, B.W. Sheldon, N.P. Padture, Fracture, fatigue, and sliding-wear behavior of nanocomposites of alumina and reduced graphene-oxide, Acta Mater. 186 (2020) 29–39.
23. A.K. Suri, C. Subramanian, J.K. Sonber, T.S.R.-Ch. Murthy, Synthesis and consolidation of boron carbide: a review, Int. Mater. Rev. 55 [1] (2010) 4–40.
24. S.L. Dole, S. Prochazka, R.H. Doremus, Microstructural coarsening during sintering of boron carbide, J. Am. Ceram. Soc. 72 [6] (1989) 958–966.
25. W. Ji, R.I. Todd, W. Wang, H. Wang, J. Zhang, Z. Fu, Transient liquid phase spark plasma sintering of B_4C-based ceramics using Ti-Al intermetallics as sintering aid, J. Eur. Ceram. Soc. 36 [10] (2016) 2419–2426.
26. A.L. Ortiz, C.A. Galán, O. Borrero-López, F. Guiberteau, Highly sliding-wear resistant B_4C

composites fabricated by spark-plasma sintering with Ti-Al additives, Scripta Mater 177 (2020) 91–95.

27. C. Ojalvo, R. Moreno, F. Guiberteau, A.L. Ortiz, Manufacturing B_4C parts with Ti-Al intermetallics by aqueous colloidal processing, J. Eur. Ceram. Soc. 40 [2] (2020) 226–233.
28. C. Ojalvo, F. Guiberteau, A.L. Ortiz, Fabricating toughened super-hard B_4C composites at lower temperature by transient liquid-phase assisted spark plasma sintering with $MoSi_2$ additives, J. Eur. Ceram. Soc. 39 [9] (2019) 2862–2873.
29. A.L. Ortiz, V.M. Candelario, R. Moreno, F. Guiberteau, Near-net shape manufacture of B_4C–Co and ZrC–Co composites by slip casting and pressureless sintering, J. Eur. Ceram. Soc. 37 [15] (2017) 4577–4584.
30. S. Eqtesadi, A. Motealleh, F.H. Perera, P. Miranda, A. Pajares, R. Wendelbo, F. Guiberteau, A.L. Ortiz, Fabricating geometrically-complex B_4C ceramic components by robocasting and pressureless spark plasma sintering, Scripta Mater 145 (2018) 14–18.
31. R. Moreno, Reología de suspensiones cerámicas, Consejo Superior de Investigaciones Científicas, Madrid, Spain, 2005.
32. R. Moreno, Better ceramics through colloid chemistry, J. Eur. Ceram. Soc. 40 [3] (2020) 559–587.
33. J.S. Reed, Principles of ceramics processing, John Wiley and Sons, New York, US, 1995.
34. S. Leo, C. Tallon, G.V. Franks, Aqueous and nonaqueous colloidal processing of difficult-to-densify ceramics: suspension rheology and particle packing, J. Am. Ceram. Soc. 97 [12] (2014) 3807–3817.
35. B.M. Moshtaghioun, F.L. Cumbrera-Hernández, D. Gómez-García, S. de Bernardi-Martín, A. Domínguez-Rodríguez, A. Monshi, M.H. Abbasi, Effect of spark plasma sintering

parameters on microstructure and room-temperature hardness and toughness of fine-grained boron carbide (B_4C), J. Eur. Ceram. Soc. 33 [2] (2013) 361–369.

36. A. Motealleh, A.L. Ortiz, O. Borrero-López, F. Guiberteau. Effect of hexagonal-BN additions on the sliding-wear resistance of fine-grained α-SiC densified with $Y_3Al_5O_{12}$ liquid phase by spark-plasma sintering, J. Eur. Ceram. Soc. 34 [3] (2014) 565–574.
37. V.M. Candelario, O. Borrero-López, F. Guiberteau, R. Moreno, A.L. Ortiz, Sliding-wear resistance of liquid-phase-sintered SiC containing graphite nanodispersoids, J. Eur. Ceram. Soc. 34 [10] (2014) 2597–2602.
38. V.M. Candelario, R. Moreno, F. Guiberteau, A.L. Ortiz, Enhancing the sliding-wear resistance of SiC nanostructured ceramics by adding carbon nanotubes, J. Eur. Ceram. Soc. 36 [13] (2016) 3083–3089.
39. V.M. Candelario, R. Moreno, Z. Shen, F. Guiberteau, A.L.Ortiz, Liquid-phase assisted spark-plasma sintering of SiC nanoceramics andtheir nanocomposites with carbon nanotubes, J. Eur. Ceram. Soc. 37 [5] (2017) 1929–1936.
40. B.M. Moshtaghioun, D. Gómez-García, A. Domínguez-Rodríguez, A.L. Ortiz, Enhancing the spark-plasma sinterability of B_4C nanopowders via room-temperature methylation induced purification, J. Eur. Ceram. Soc. 36 [11] (2016) 2843–2848.
41. A.L. Ortiz, F. Sánchez-Bajo, V.M. Candelario, F. Guiberteau, Comminution of B_4C powders with a high-energy mill operated in air in dry or wet conditions and its effect on their spark-plasma sinterability, J. Eur. Ceram. Soc. 37 [13] (2017) 3873–3884.

Figure Captions

Figure. 1. Schematic illustration of the experimental assembly of the graphite tools used for PSPS. The different elements are indicated.

Figure 2. Dependence of the viscosity on the shear rate for the semi-concentrated slurry of 89.82B_4C+7.08Ti-Al+3.10prGO prepared to a total solids loading of 20 vol.% and sonicated for 2 min, and optical photograph showing its visual appearance (inset). The arrows indicate the uploading and downloading stretches of the viscosity curve.

Figure 3. Optical photographs of some compacts prepared by slip casting, taken (A) during their drying within the moulds and (B) once dried.

Figure 4. SEM image (23 500×) of the fracture surface of the green compacts showing their microstructure in the as-cast and dried conditions (prior to isostatic pressing).

Figure 5. Degrees of linear and volume shrinkages undergone by the green compacts as a function of the sintering temperature. The solid lines are guides for the eye.

Figure 6. SEM micrographs of the fracture surface of the B_4C/rGO composites sintered at (A) 1900°C (10 000×), (B) 1950°C (10 000×), (C) 2000°C (5000×), (D) 2050°C (5000×), and (E) 2100°C (2000×) for 5 min.

Figure 7. SEM micrograph of B_4C/rGO composite sintered at 2100°C for 5 min, taken at higher magnification (20 000×). rGO reinforcements are marked with arrows.

Figure 8. Hardness of the B_4C/rGO composites as a function of the sintering temperature. The solid line is a guide for the eye.

Figure

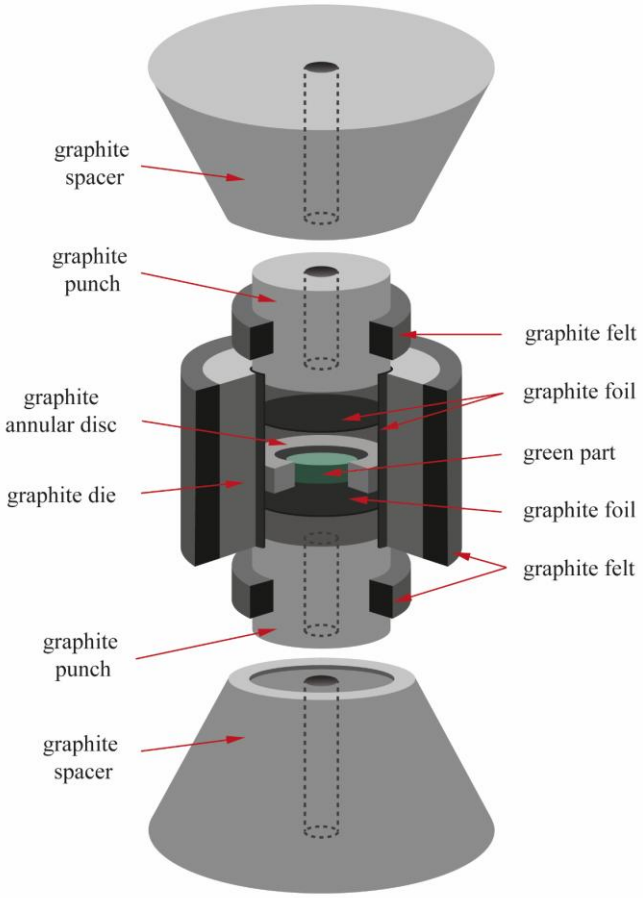

Ojalvo *et al.*
Figure 1

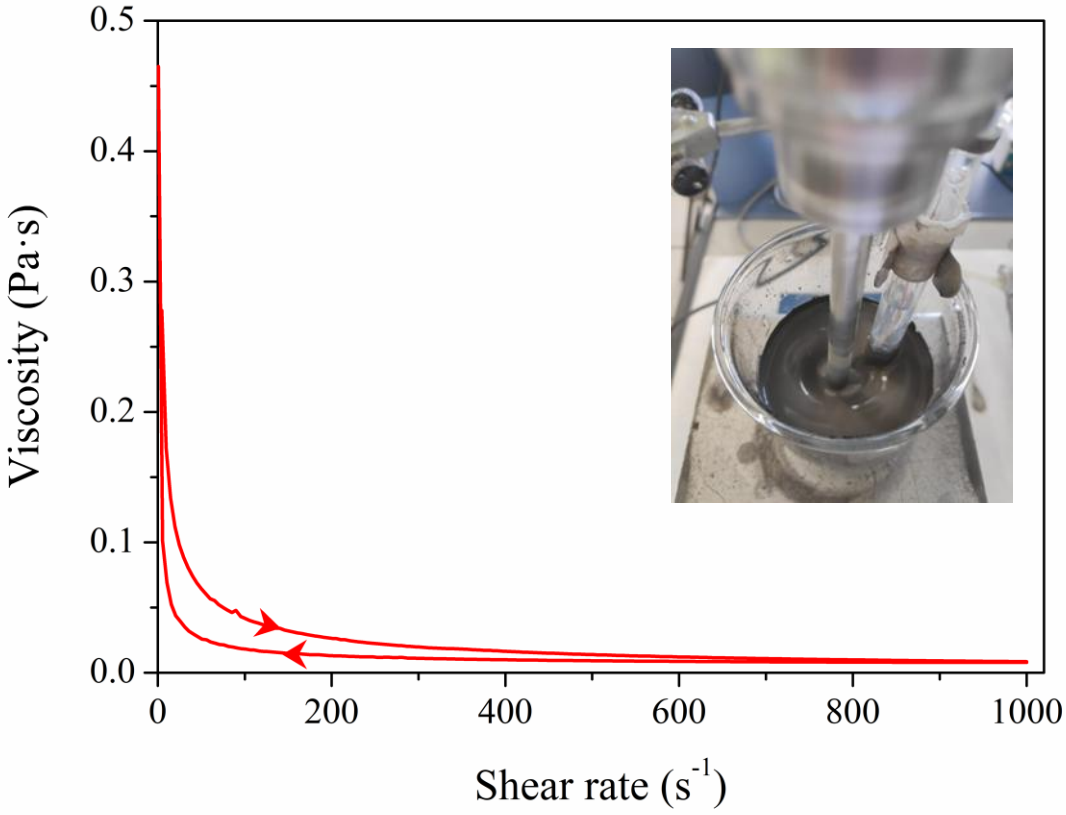

Ojalvo *et al.*
Figure 2

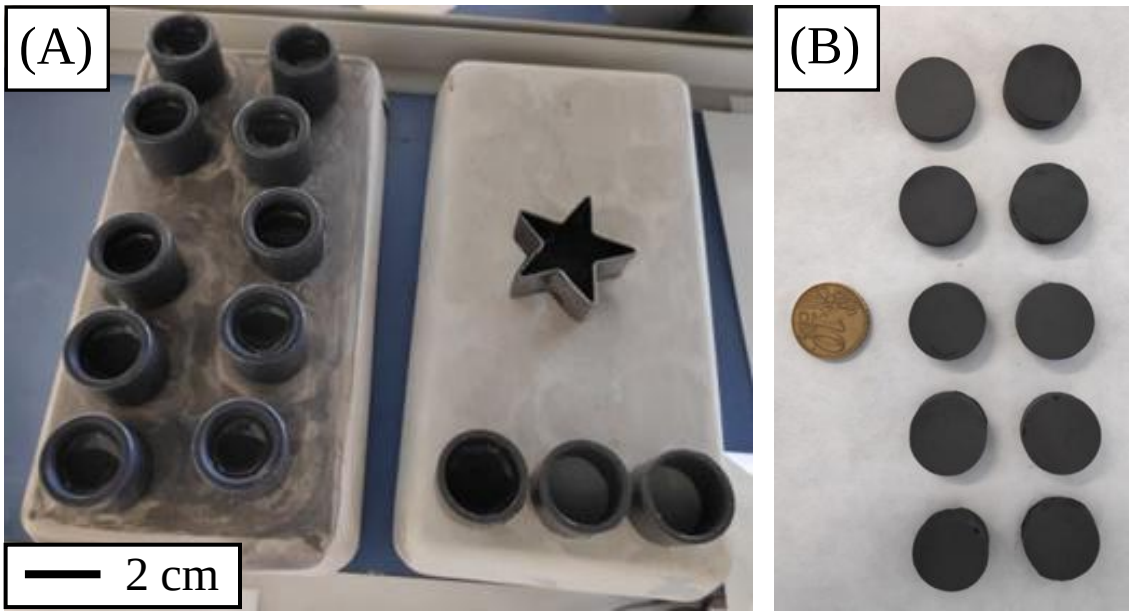

Ojalvo *et al.*
Figure 3

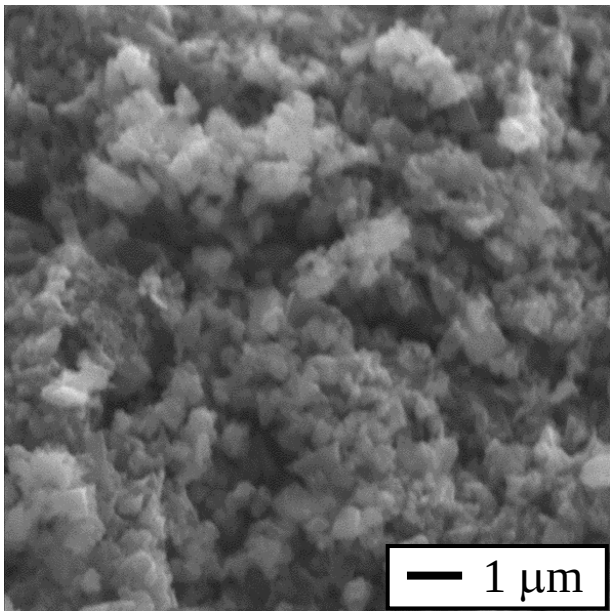

Ojalvo *et al.*
Figure 4

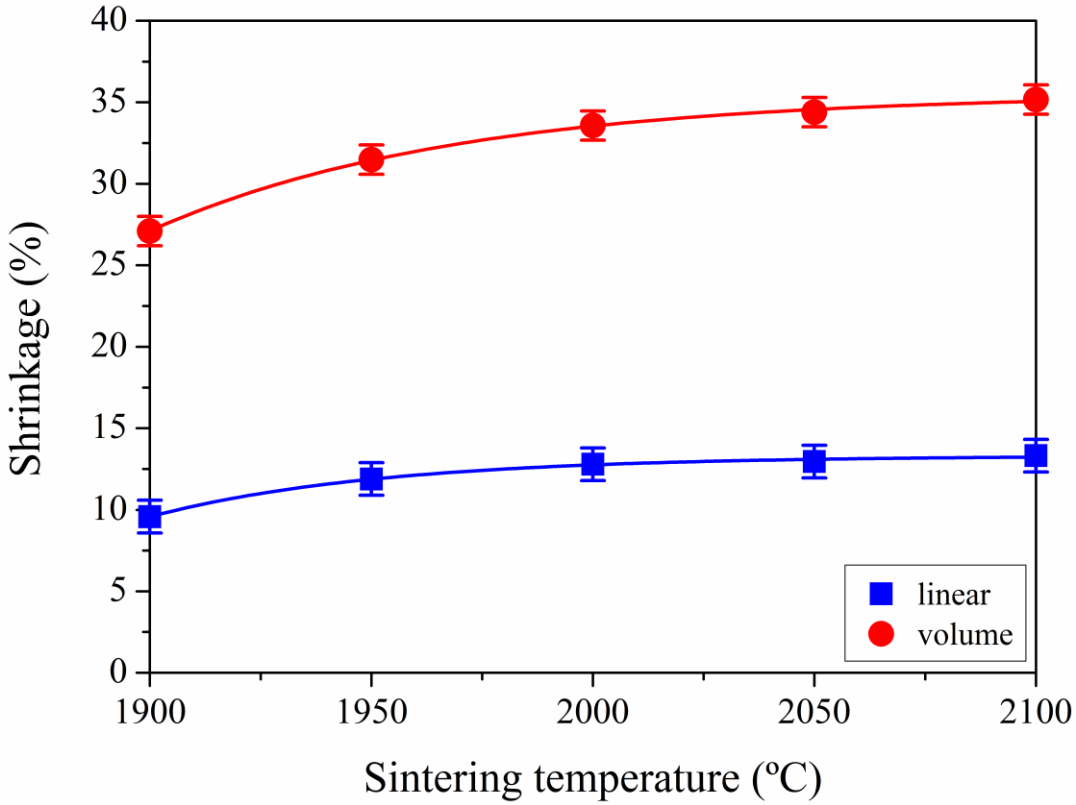

Ojalvo *et al.*
Figure 5

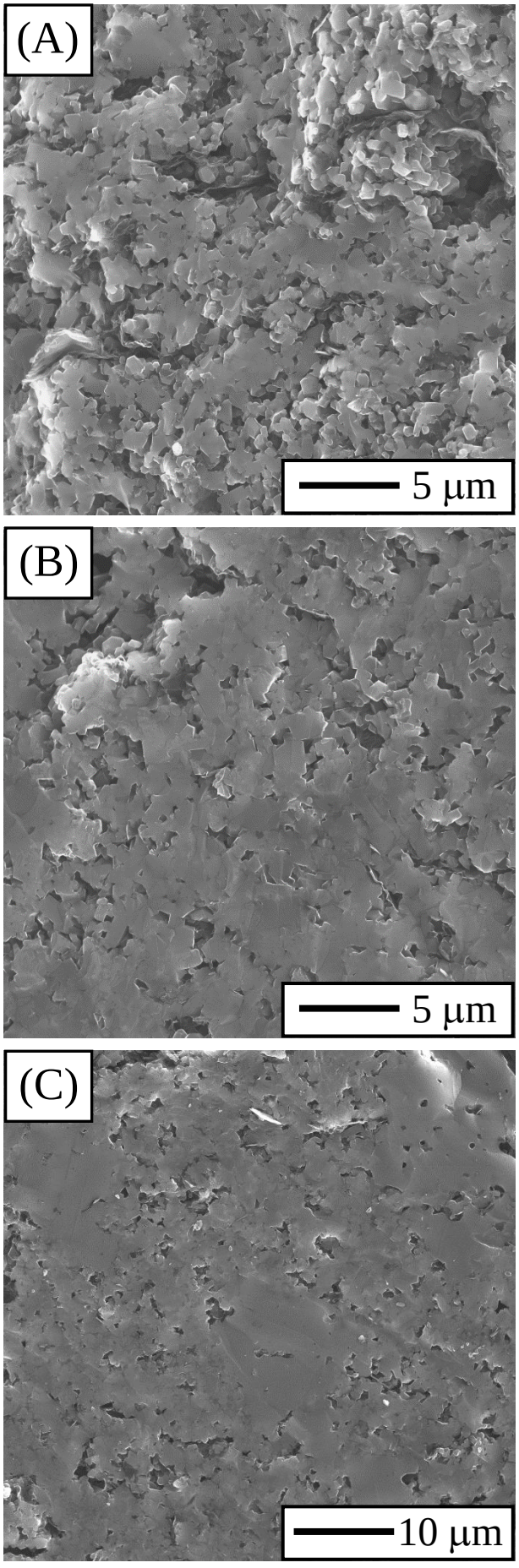

Ojalvo *et al.*
Figure 6

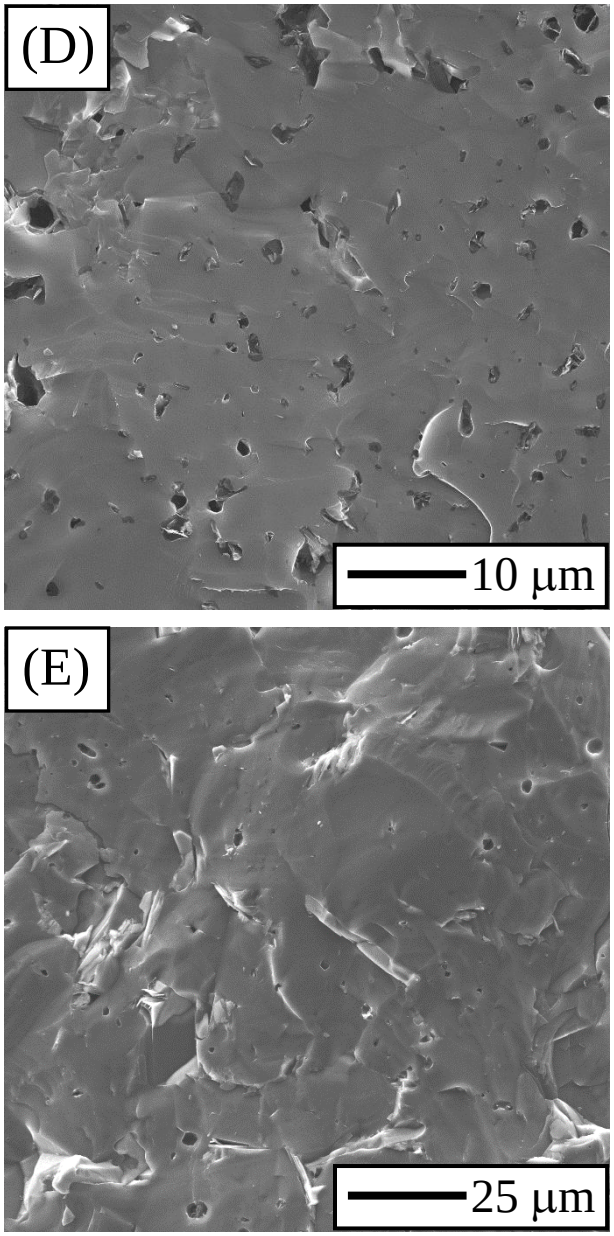

Ojalvo *et al.*
Figure 6

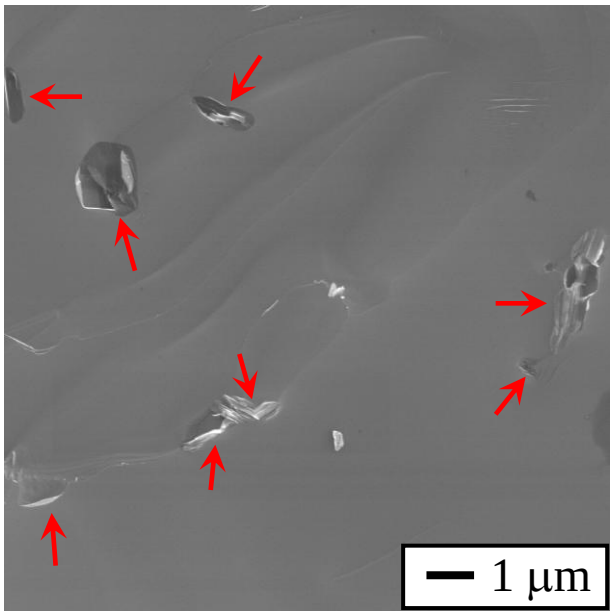

Ojalvo *et al.*
Figure 7

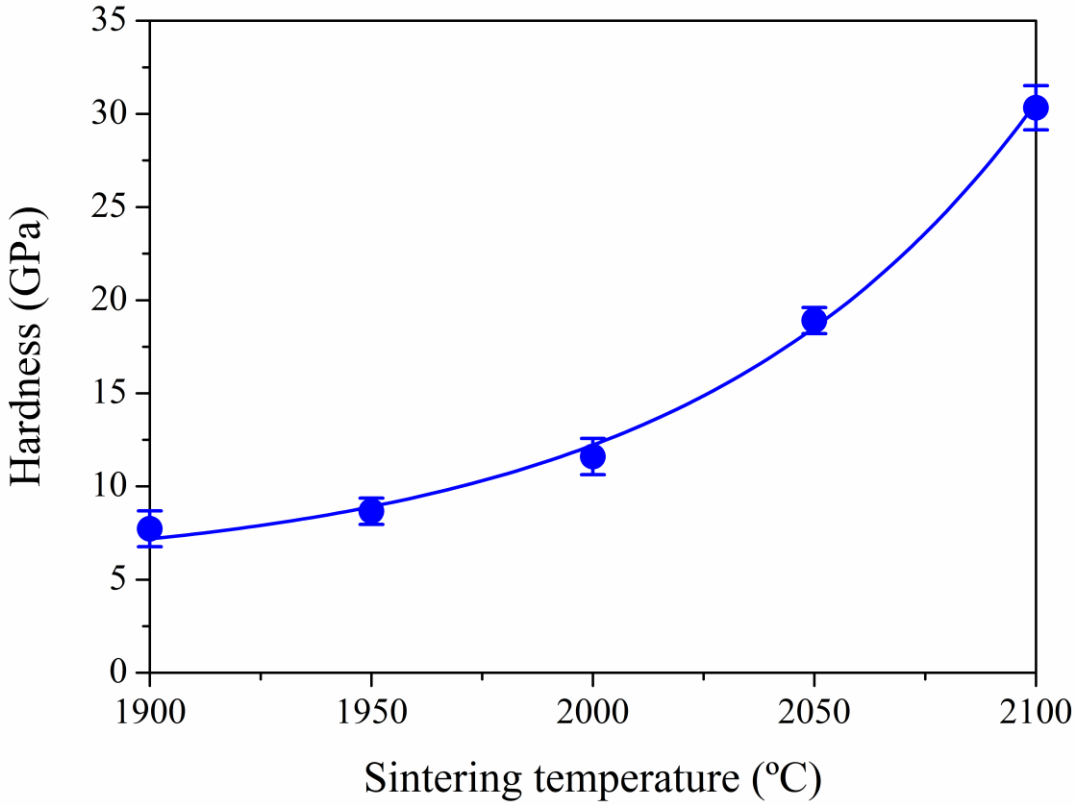

Ojalvo *et al.*
Figure 8

Figure Captions

Figure. 1. Schematic illustration of the experimental assembly of the graphite tools used for PSPS. The different elements are indicated.

Figure 2. Dependence of the viscosity on the shear rate for the semi-concentrated slurry of 89.82B_4C+7.08Ti-Al+3.10prGO prepared to a total solids loading of 20 vol.% and sonicated for 2 min, and optical photograph showing its visual appearance (inset). The arrows indicate the uploading and downloading stretches of the viscosity curve.

Figure 3. Optical photographs of some compacts prepared by slip casting, taken (A) during their drying within the moulds and (B) once dried.

Figure 4. SEM image (23 500×) of the fracture surface of the green compacts showing their microstructure in the as-cast and dried conditions (prior to isostatic pressing).

Figure 5. Degrees of linear and volume shrinkages undergone by the green compacts as a function of the sintering temperature. The solid lines are guides for the eye.

Figure 6. SEM micrographs of the fracture surface of the B_4C/rGO composites sintered at (A) 1900°C (10 000×), (B) 1950°C (10 000×), (C) 2000°C (5000×), (D) 2050°C (5000×), and (E) 2100°C (2000×) for 5 min.

Figure 7. SEM micrograph of B_4C/rGO composite sintered at 2100°C for 5 min, taken at higher magnification (20 000×). rGO reinforcements are marked with arrows.

Figure 8. Hardness of the B_4C/rGO composites as a function of the sintering temperature. The solid line is a guide for the eye.

***Summary of Novel Conclusions**

- Superhard composites of B_4C reinforced with randomly-oriented reduced graphene oxide (rGO) nanoplatelets are manufactured with near-net shape.
- The fabrication route is simple and environmentally friendly, and uses aqueous slip casting to obtain robust green parts with shape on demand and pressureless spark plasma sintering for their ultrafast densification with shape retention.
- The isotropic B_4C/rGO composites sintered at 2100°C are superhard and almost twice as tough as the monolithic B_4C ceramics.